Texture evolution in Nd:YAG-laser welds of AZ31 magnesium alloy hot rolled sheets and its influence on mechanical properties

Loreleï Commin[a,*], Myriam Dumont[b], René Rotinat[a], Fabrice Pierron[a], Jean-Eric Masse[c], Laurent Barrallier[c]

[a] LMPF, Arts et Metiers ParisTech, rue St Dominique, 51000 Châlons en Champagne, France
[b] IM2NP, Université Cézanne, Avenue Escadrille Normandie Niemen, 13 397 Marseille, France
[c] MécaSurf, Arts et Metiers ParisTech, 2 cours des Arts et Métiers, 13100 Aix en Provence, France

A B S T R A C T

AZ31 hot rolled magnesium alloy presents a strong basal texture. Using laser beam welding (LBW) as a joining process induces high temperature gradients leading to major texture changes.

Electron back scattered diffraction (EBSD) was used to study the texture evolution, and tensile tests coupled with speckle interferometry were performed to understand its influence on mechanical properties. The random texture obtained in the LBW fusion zone is mainly responsible for the yield strength reduction.

Keywords:
Laser welding
Magnesium alloys
XRD
EBSD
Mechanical properties

1. Introduction

Magnesium alloys are raising more and more interest in structural applications due to their high specific properties. Joining is one of the manufacturing routes that can be used to optimise product design and minimise production costs, but its use still faces many challenges. Traditional welding techniques are difficult to perform and the manufacturing process that is most commonly used is gas tungsten arc welding (GTAW).

However, as this process results in a high level of porosity and weld deformation, other welding techniques have to be considered [1].

Laser beam welding (LBW) seems to be a suitable technique to be used for joining magnesium alloys as it presents a low and precise heat input, high welding speed and a small heat affected zone (HAZ) [1]. LBW induces metal fusion and high temperature gradients which may cause changes in microstructure and crystalline orientations and lead to residual stress generation. The study of the microstructure and texture evolution is therefore required to understand the evolution of mechanical properties.

The magnesium alloy studied here is AZ31 in hot-rolled condition.

Recent studies have been conducted on AZ31 CO_2 laser welds [2–4] using conventional tensile tests. They reported the global influence of microstructural changes occurring in the fusion zone (FZ).

In this study, a local analysis was performed. Full field measurement techniques allow the investigation of the contribution of each microstructural area in the mechanical behaviour of the weld. The local texture evolution in hot rolled AZ31 caused by Nd:YAG LBW was analysed using electron backscattered diffraction (EBSD). Its influence on the weld mechanical behaviour was compared to the influence of the other microstructural features such as grain morphology, precipitation state and the influence of residual stress variations.

2. Experimental procedures

2.1. Material and processing

The base material used is 2 mm thick hot rolled sheets of AZ31–O magnesium alloy supplied by Salzgitter Magnesium Technologies (Table 1). Nd:YAG butt welding of AZ31 was carried out using 2.4 kW power and 7 m min^{-1} welding speed. Argon gas shielding was used at 30 l min^{-1}. The welding direction was parallel to the rolling direction.

As-welded samples were studied. The effect of 1 h at 300 °C post-weld heat treatment was also investigated. This heat treatment was

* Corresponding author. Fax: +33 4 42 254 990.
E-mail address: lorelei.commin@cea.fr (L. Commin).

doi:10.1016/j.msea.2010.11.061

Table 1
Chemical composition of AZ31 alloy (Salzgitter Magnesium Technologies data).

Element	Al	Zn	Mn	Si	Cu	Ni	Fe	Ca	Other	Mg
wt.%	2.5–3.5	0.6–1.4	0.2–0.6	<0.05	<0.008	<0.002	<0.005	<0.02	<0.3	Balance

chosen following [5] which reported that the mechanical properties would not be further improved by increasing either the annealing temperature or time.

2.2. Microscopy observations

Optical microscopy, scanning electron microscopy (SEM) and transmission electron microscopy (TEM) were used to characterise the precipitation state at different scales. Electron back scattered diffraction (EBSD) was used to determine the grain size (with a 3° misorientation angle threshold) and texture evolutions.

For optical and SEM observations, polished samples were etched with an acetopicral solution (0.4 g picric acid, 13 ml ethanol, 3 ml glacier acetic acid and 3 ml boiled water). They were observed using a Leitz Aristomet optical microscope and a JEOL JMS 6400 Scanning Electron Microscope (SEM).

For EBSD analysis, SEM was coupled with an HKL EBSD Camera. The samples were mechanically polished using SiC paper from 400 to 2500 grit and final polishing was performed using a 0.05 μm alumina suspension. The etchant solution used for EBSD was 10 ml nitric acid, 30 ml acetic acid, 40 ml boiled water, 120 ml ethanol for 10 s [6]. A 20 kV electron beam, 10 nA probe current and a 40 ms integration time were used. TEM was performed using a FEI TECNAI G^2 coupled with energy dispersive spectroscopy (EDS) for chemical analysis. TEM samples were prepared using a Struers Tenupol-3 jet polisher with a 14 V polishing voltage. The polishing solution was 10% HCl, 90% butoxy-2-ethanol by volume.

2.3. X-ray diffraction

X-ray diffraction (XRD) was performed using a SEIFERT MZ6TS diffractometer with Cr Kα radiation ($\lambda = 0.228975$ nm) and a position sensitive detector (PSD). Residual stress profiles were investigated. The {2 0 2} diffracting plane and $\sin^2\psi$ analysis method were used [7]. Previous studies on 2 mm thick plates showed that in-depth residual stresses obtained in the fusion zone were similar to the ones obtained on the surface [2]. Therefore, XRD analysis was limited to the sample surface (i.e. no in-depth analysis using material removal was performed).

2.4. Mechanical characterisation

Microhardness tests were performed using a Leica VMHT coupled with a Sony IRIS CCD.

The sample preparation method was the same as that used for optical micrographs.

A 0.98 N load was applied during 15 s for each indentation. Three measurements were taken to determine the error bars.

To capture the heterogeneity of deformation of the materials, tensile tests were coupled with the speckle interferometry full-field technique. Speckle interferometry is a technique which allows the in-plane and out-of-plane deformation measurement of an object surface. When a rough surface is illuminated by a beam of coherent light (in practice, a laser beam), this surface reflects the light in all directions according to the principle of Huygens–Fresnel. Speckle patterns are then obtained due to the interference of the back-scattered light.

A Q300 Dantec Ettemeyer speckle interferometry system was used (1380×1040 pixels CCD sensor, 2×70 mW/785 nm wave length laser diodes, 100 nm in-plane sensitivity, 30 nm out-of-plane sensitivity). A layer of diffusive paint was applied to the sample surface to increase diffusive reflection. The test set up consisted of a small in-house developed tensile stage.

The measurement of the phase variation between two speckle images (i.e. steps of loading) allows the calculation of out-of-plane displacement. To measure in-plane displacements, two beams are used. The phase variation gives a first component of in-plane displacement. By using an identical setup rotated by 90° one obtains the other component of in-plane displacement. The displacement resolution is close to 0.1 μm for a spatial resolution of about 16 μm. Strains were obtained from displacements using a diffuse approximation filtering (radius = 20 pixels, 248 μm resolu-

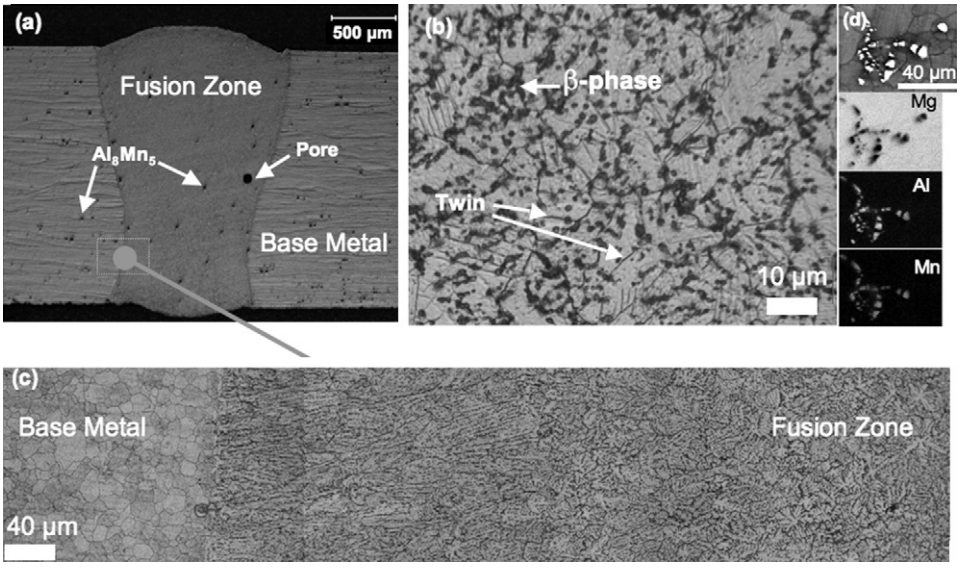

Fig. 1. Optical micrographs of (a) the weld section, (b) the fusion zone and (c) the base metal-fusion zone transition. (d) SEM image and corresponding EDS maps of Al_8Mn_5 precipitates in BM.

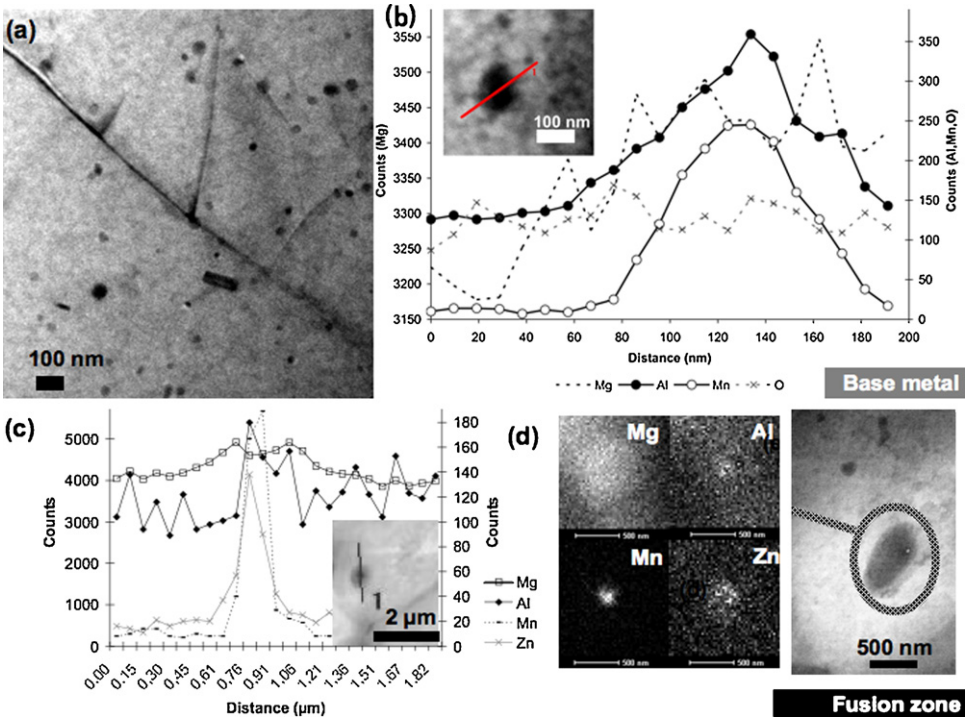

Fig. 2. (a) TEM BF image of Al_8Mn_5 nanoprecipitation in BM, (b) EDS maps of Al_8Mn_5 nanoprecipitation in BM, (c) EDS analysis across a precipitate observed within the FZ. (d) EDS map and TEM BF image of a precipitate observed within the FZ.

tion) that provides excellent reconstruction/filtering compromise as described in [8,9]. The strain resolution is 2×10^{-5}.

Conventional tensile tests were performed at 4 mm min^{-1} strain rate using an Instron 1185 machine with mechanical grips. Five specimens were tested for repeatability.

3. Results

3.1. As-welded samples

3.1.1. Weld microstructure—grain size and precipitation evolution

The LBW microstructure differs in three different zones: the base metal (BM), the heat affected zone (HAZ) and the fusion zone (FZ).

The BM consists in 10 μm α-Mg equiaxed grains containing Al_8Mn_5 precipitates and without twinning (Fig. 1). In this study, the HAZ could not be distinguished using microscopy: as can be seen in Fig. 1(c), the transition BM/FZ is very abrupt; in particular no liquation at grain boundaries can be observed.

Concerning the FZ, its microstructure presented a dendritic like morphology consisting of the α-Mg phase, the Al_8Mn_5 intergranular precipitation and an additional phase (Fig. 1(a)). The dendrites were equiaxed in the central areas which last solidified, whereas columnar dendrite structure was observed at the BM boundary where the temperature gradients were higher (Fig. 1(c)). The additional phase morphology consisted of small dark particle agglomerates distributed along the α-Mg grain boundaries but also within the α-Mg phase (Fig. 1(b)). This dendritic-like microstructure observed in the LBW fusion zone is consistent with previous studies [3] and is similar to the one observed in rapidly solidified AZ31 [5].

A TEM study was performed to investigate precipitation at the sub-micrometer scale. In the BM, only nanosized Al_8Mn_5 precipitation was observed (Fig. 2(a) and (b)). In the FZ, large particles were observed (Fig. 2(c) and (d)) with a size ranging from 500 to 1500 nm. In most cases, they were containing smaller 50–150 nm particles. EDS was used to identify the nature of these precipitates (Fig. 2(c) and (d)). It indicated that there was an increase in Al and Mn content in the small particles, surrounded by an Al–Mg–Zn rich area. During LBW, rapid solidification occurred and the maximum solubility of aluminium decreased quickly, causing the precipitation of the remaining aluminium in $Mg_{17}(Al, Zn)_{12}$ β-phase. The 50–150 nm particles could be identified as Al_8Mn_5.

Considering the grain structure, the presence of the β-phase in the FZ prevented grain observation using conventional microscopy (Fig. 1(b)). The grain size evolution was then studied using EBSD (Fig. 3). The grain size in the FZ was similar to that found in the base metal. Moreover, twinning occurred in the FZ (Fig. 1(b)).

3.1.2. Weld microstructure—texture evolution

EBSD was used to study the local texture evolution across the LBW. The analysis was performed on the weld cross section. EBSD results showed that whereas the base material exhibits a strong texture, the material in the fusion zone is not textured (Fig. 3). Indeed, the grains in the base metal area exhibit a strong basal texture. The {0 0 2} basal plane normal was parallel to the sample normal direction, as the analysis was performed in the sample section. A random colouring in Fig. 3(c) is obtained in the fusion zone characterizing a random orientation of the equiaxed grains.

3.1.3. Mechanical properties

The weld quality was assessed using optical micrographs. It should be noted that very little porosity was observed in the FZ of the weld, the dark spots being mainly Al_8Mn_5 precipitates (Fig. 1(a)). The mechanical properties of the samples are therefore characteristic of the material.

The results of microhardness measurements are shown in Fig. 4. A larger scatter of the values is obtained in the fusion zone, due to the microstructural heterogeneity in this area. Higher microhardness values were measured in the FZ and lower values in the FZ edges. But these evolutions are within the errors bars. Therefore, the microhardness is only slightly influenced during welding.

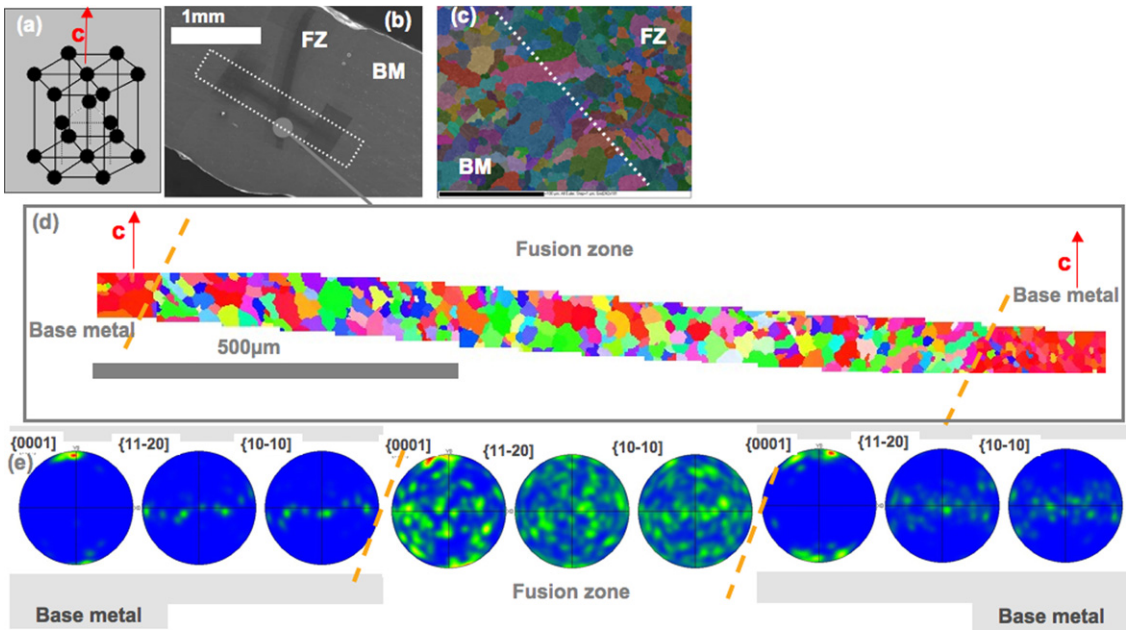

Fig. 3. (a) Sketch of the hep crystal, (b) location of the analysis, (c) EBSD maps of the FZ/MB transition, (d) EBSD maps of the LBW section (IPF colouring), and (e) corresponding pole figures.

Regarding the thermal history, large variations of internal stresses can be expected along the weld that may influence the mechanical properties of the weld piece. Therefore, residual stress variations along the weld were investigated. Fig. 5 displays the residual stress tensor determined by $\sin^2\psi$ method in the base metal and the fusion zone. It shows that whereas compressive stresses dominate in the base metal, tensile stresses developed in the fusion zone. This was attributed to the shrinkage during rapid cooling. These results are consistent with the AZ31 CO_2 LBW Coelho et al. study [2] which observed 40 MPa tensile residual stresses in the fusion zone.

During conventional tensile tests, LBW butt welds showed similar ultimate tensile strength (UTS) but lower yield strength (YS) and strain to failure compared to the base metal (Fig. 6). The fracture occurred each time in the base metal.

Tensile tests were then coupled with the speckle interferometry technique to investigate the local mechanical behaviour evolution in each zone (Fig. 7).

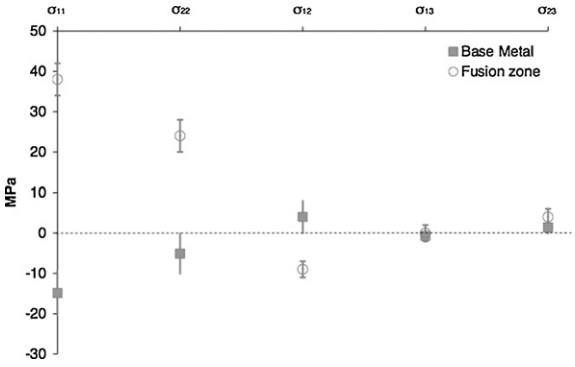

Fig. 5. Residual stress tensor evolution between the BM and the FZ, with 1 the longitudinal direction, 2 the transverse direction and 3 the normal direction of the weld.

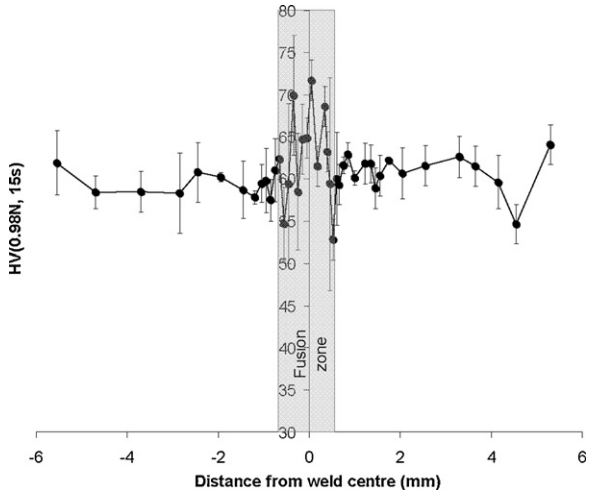

Fig. 4. Microhardness evolution across the LBW, the shaded area represents the FZ.

Strain localisation occurred first in the weld area (Fig. 7(a)) and then within the base metal in bands perpendicular to the loading direction (Fig. 7(b)). The formation of this type of pattern after loading in hot-rolled AZ31, constituted by a high amount of twins, was described by Barnett et al. [10]. The fracture finally occurs in these areas within the BM.

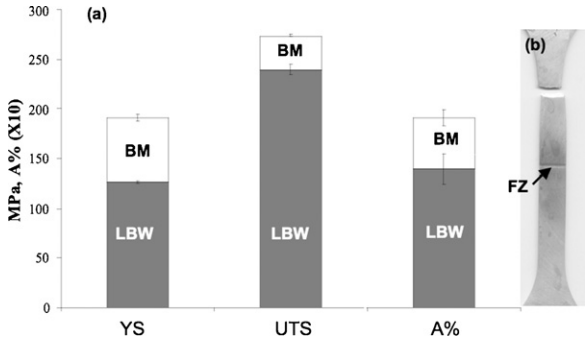

Fig. 6. (a) Conventional tensile properties of the LBW compared to the BM ones, the error bars represent ± one standard deviation. (b) Fractured sample.

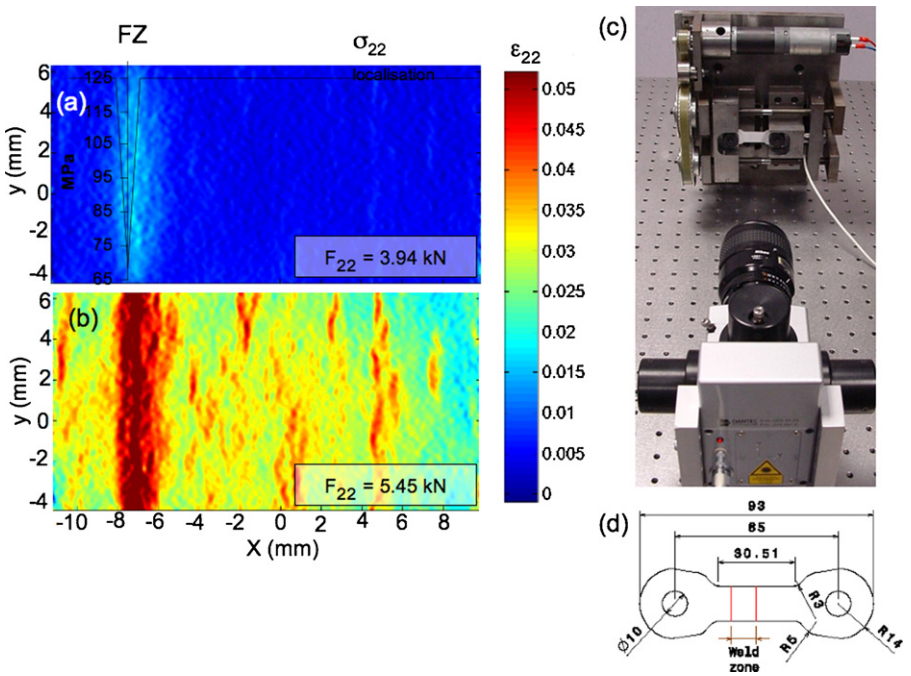

Fig. 7. ε_{22} maps from speckle interferometry (a) at $F = 3.94$ kN, with σ_{22} localisation superimposed, (b) at $F = 5.45$ kN, with the same axis convention as the residual stress analysis, (c) experimental set-up, and (d) specimen geometry.

As the mechanical behaviour is different in the FZ and the BM, the tensile load at which strain localisation occurs is different in each zone. This can be observed in speckle analysis deformation maps (Fig. 7), each map corresponding to a specific tensile load applied. Strain localisation occurs first in the FZ at $F = 2.75$ kN tensile load and then at $F = 5$ kN tensile load in the BM. The tensile stresses associated to these loads can be calculated ($\sigma_{22\ \text{localisation}}$) and are displayed in Fig. 7(a).

3.2. Post-weld heat treated samples

Post weld heat treatment was carried out to try to recover mechanical properties of the base metal. After post-weld heat treatment (300 °C, 1 h), optical microstructure and mechanical properties, using conventional tensile tests, were investigated. It showed that the mechanical properties of the weld can be improved after annealing. The fracture still occurred in the BM. The strain to failure and UTS were restored whereas the yield strength remained lower than that in the BM (Fig. 8(a)).

After post-weld heat treatment the FZ microstructure has changed (Fig. 8(b)). The $Mg_{17}(Al,Zn)_{12}$ phase dissolved in the α-Mg matrix. The grain size could then be analysed using optical microscopy and it was observed that it had remained similar. This was also described by Ju et al. after heat treating of rapidly solidified AZ31 [5].

4. Discussion

The welds studied here did not suffer large porosity content and therefore, the mechanical properties obtained describe the material and are not resulting from weld defect influence. LBW resulted in lower mechanical properties, which was also reported in previous studies [1,2,4].

The evolution of mechanical properties can be attributed to the microstructural modification (β-phase formation, precipitate evolution, texture evolution) or to the residual stress state modification. In this section the comparative contribution of these mechanisms will be investigated.

4.1. Yield strength evolution

The Al_8Mn_5 precipitation was not modified during LBW. Indeed, Al_8Mn_5 nanoprecipitation in the FZ exhibited the same morphology as that observed in the BM. Moreover, the $Mg_{17}(Al–Zn)_{12}$ phase surrounded it. The AZ31/Mn phase diagram [11] for a Mn content between 0.2 and 0.6% presents a liquid + Al_8Mn_5 area in the 610–660 °C range. Therefore, during solidification, the nanosized precipitates initially observed in the AZ31 base metal serve as nucleation sites for the β-phase. This is consistent with the Tamura study [12], which found that β precipitates preferentially formed in the Mn-rich areas. Moreover, during β-phase formation, some Al atoms can be replaced by Zn atoms, then leading to $Mg_{17}(Al–Zn)_{12}$ compound [12]; in fact, diffusivity of Zn in Mg is higher than the diffusivity of Al in Mg.

The grain size was not modified both after LBW and after post-weld heat treatment.

Then, the $Mg_{17}(Al, Zn)_{12}$ precipitation and the twinning occurring in the fusion zone may act as hardening mechanisms and might be responsible for the slight microhardness increase.

The β-phase which had formed during LBW had dissolved after post-weld heat treatment without modifying the yield strength of the sample. Therefore, the β-phase evolution cannot be responsible for the yield strength evolution consecutive to LBW.

The residual stress state influence on the yield stress evolution can be analysed using $\sigma_{\text{localisation}}$ determined by speckle interferometry (Fig. 7) and the residual stress tensor calculated in each zone (Fig. 5). Indeed, the local material yield stress can be approximated by the equivalent stress (Von Mises) resulting from the residual stress tensor and the tensile localisation stress tensor ($\sigma_{\text{localisation}}$).

The applied tensile stress is considered as uniaxial whereas the residual stresses are multiaxial. Therefore a tensile stress component corresponding to $\sigma_{22\ \text{localisation}}$ was added to the residual stress corresponding component: $\sigma_{22} = \sigma_{22}\,(\text{residual}) + \sigma_{22\ \text{localisation}}$, with the loading direction being the weld transverse direction, labelled direction 2.

Then, the resulting equivalent stress (Von Mises) was calculated and assumed to represent the local material yield stress. When

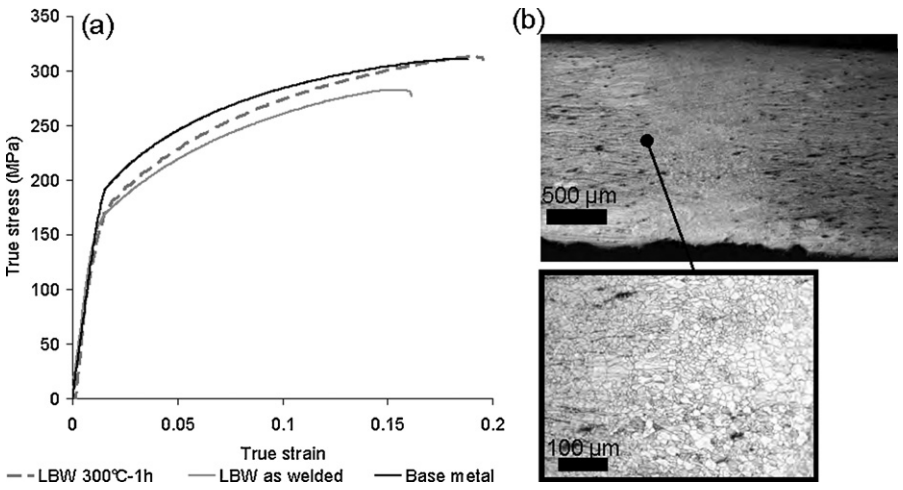

Fig. 8. (a) True stress/strain curve of post-weld heat treated LBW compared to LBW and BM curves. (b) Optical micrographs of FZ after post-weld beat treatment.

comparing it to the equivalent residual stress obtained by XRD, the residual stresses represent 35% of the material yield stress in the FZ.

Annealing treatment generally results in residual stress relief [13], but after PWHT, the yield stress was not improved. It shows that in this case, the residual stress state had not a major influence on the material mechanical behaviour.

The {0 0 2} basal texture of the BM that is characteristic of the hot rolling process [14] was dramatically modified after LBW. The resolidification process occurring in the FZ during LBW leads to the nucleation and growth of new grains and therefore, as the temperature gradient within the weld pool is small, no preferred crystalline orientation is induced in this area. This is consistent with recent results published by Yu et al. [4].

Whereas the BM strong basal texture allows very few slip systems, the random texture in the FZ presents a larger variety of grains aligned more favourably to the tensile direction. This could lead to the activation of different deformation mechanisms inducing low yielding strength [4,15]. During PWHT, the grain orientation cannot be modified without recrystallisation and, as the grain size is constant, the texture cannot be influenced by the preferential growth of specific oriented grains. Then, the texture that had developed due to LBW is still present after this PWHT and can actively influence the mechanical properties.

The lower yield stress can therefore be attributed to the texture change during LBW.

These results can be compared to those of Coelho et al. [2]. They also found, when using standard tensile test samples in the transverse direction, that the LBW presented lower yield stress than the BM. But, when using micro-flat tensile samples to study the local properties, they found a higher yield stress in the FZ than in the BM. This contradiction between the standard tensile test results and the micro-flat specimen results was not explained in their article but could be attributed to the residual stress relief occurring when producing the micro-flat tensile samples. Indeed, the difference in yield stress between their two types of samples is 46 MPa, which corresponds to the residual stress calculated in the FZ by both our studies.

4.2. Tensile strength and strain to failure evolution

Conventional tensile tests showed that the UTS dropped by about 30 MPa after LBW compared to BM. After annealing post-weld heat treatment, the UTS reached the BM value. This could be explained by the residual stress relief that had occurred during post-weld heat treatment.

After LBW, the fracture occurred each time in the BM during tensile tests, therefore, the loss in mechanical properties after LBW cannot be attributed solely to the FZ. This is in contradiction with previous studies. Yu et al. [4] which focussed on very fine grain microstructure (1.9 μm BM grain size), observed that the fracture occurred each time in the FZ. They attributed it to the grain coarsening in the FZ, which resulted in a lower hardness and a lower ability to withstand plastic deformation.

Quan et al. [3] recently attributed the loss in UTS and elongation after LBW to the microstructural change in the FZ. This explanation is not confirmed in our study. Indeed, the microstructural change is occurring in the FZ, whereas the fracture occurs in the BM.

This behaviour could be explained by the band formation and their ability to undergo deformations. Due to the, occurs under loading in the BM. In the FZ due to the random texture yielding occurs earlier but, the ductility is lower in the BM because the basal texture induces limited deformation mechanism leading to the band formation [10]. After post-weld heat treatment, the band removal is occurring due to the disappearance of twins during annealing [16]. This may have led to the UTS and strain to failure recovery.

5. Conclusions

The study of the evolution of the microstructure and mechanical behaviour of AZ31 LBW leads to several conclusions:

1. After LBW, the grain size and the Al_8Mn_5 precipitation remains similar and $Mg_{17}(Al–Zn)_{12}$ formation is observed in the fusion zone.
2. In the fusion zone, the Al_8Mn_5 nanoprecipitation acts as nucleation site for $Mg_{17}(Al–Zn)_{12}$ precipitation.
3. The strong {0 0 2} texture of AZ31 hot rolled base metal was modified by the welding process. The small temperature gradient in the weld pool produced the nucleation of randomly oriented grains in the fusion zone.
4. A reduction of the yield stress, the UTS and the elongation is observed after LBW.
5. Post-weld heat treatments are promising since a recovery of elongation and UTS can be achieved by a 300 °C/1 h heat treatment.
6. Precipitation and residual stresses evolutions had a little influence on the yield strength whereas the texture change occurring in the fusion zone is mainly responsible for the yield strength reduction.

7. The residual stresses and band feature formation during deformation are responsible of the UTS and ductility loss after LBW.

Acknowledgements

This work was performed as a part of AEROMAG Project "Aeronautical Application of Wrought Magnesium" (Project No AST4-CT-2005-516152) which was supported by the European Union. The authors wish to thank EADS-IWF, Suresnes for Laser Beam Welding, CP2M laboratory, Paul Cezanne University, Marseille for TEM facility, MecaSurf laboratory, Arts et Metiers ParisTech, Aix en Provence for EBSD and XRD facilities.

References

[1] X. Cao, M. Jahazi, J.P. Immarigeon, J. Mater. Process. Technol. 171 (2006) 188–204.
[2] R.S. Coelho, A. Kotska, H. Pinto, S. Riekehr, M. Koçak, A.R. Pyzalla, Mater. Sci. Eng. A 485 (2008) 20–30.
[3] Y.J. Quan, Z.H. Chen, X.S. Gong, Z.H. Yu, Mater. Charact. 59 (2008) 1491–1497.
[4] L. Yu, K. Nakata, N. Yamamoto, J. Liao, Mater. Lett. 63 (2009) 870–872.
[5] D.Y. Ju, X.D. Hu, Trans. Non Ferrous Met. Soc. China 16 (2006) 874–877.
[6] Z. Keshavarz, M.R. Barnett, Scripta Mater. 55 (2006) 915–918.
[7] L. Castex, J.L. Lebrun, G. Maeder, J.M. Sprauel, Pub. Sci. et Tech. ENSAM (1981).
[8] B. Nayroles, G. Touzot, P. Villon, Comput. Mech. 10 (1992) 307–318.
[9] S. Avril, P. Feissel, F. Pierron, P. Villon, Eur. J. Comput. Mech. 17 (2008) 857–868.
[10] M.R. Barnett, N. Stanford, Scripta Mater. 57 (2007) 1125–1128.
[11] T. Laser, M.R. Nürnberg, A. Janz, C. Hartig, D. Leitzig, R. Schmid-Fetzer, R. Bormann, Acta Mater. 54 (2006) 3033–3041.
[12] Y. Tamura, Y. Kida, H. Tamehiro, N. Kono, H. Soda, A. McLean, J. Mater. Sci. 43 (2008) 1249–1258.
[13] P. Sedek, J. Brozda, L. Wand, P.J. Withers, Int. J. Pressure Vessels Piping 80 (2003) 705–713.
[14] W Woo, H. Choo, D.W. Brown, P.K. Liaw, Z. Feng, Scripta Mater. 54 (2006) 1859–1864.
[15] S.R. Agnew, J.A. Horton, T.M. Lillo, D.W. Brown, Scripta Mater. 50 (2004) 377–381.
[16] S. Yi, I. Schestakow, A. Zaefferer, Mater. Sci. Eng. A 516 (2009) 58–64.